Journal of Energy Chemistry 54 (2021) 208–216

Contents lists available at ScienceDirect

Journal of Energy Chemistry

journal homepage: www.elsevier.com/locate/jechem

http://www.journals.elsevier.com/journal-of-energy-chemistry/

Effects of structure and electronic properties of D-π-A organic dyes on photovoltaic performance of dye-sensitized solar cells

Min-Woo Lee [a,1], Jae-Yup Kim [b,1], Hyung-Geun Lee [c], Hyun Gil Cha [a], Duck-Hyung Lee [c,*], Min Jae Ko [d,e,*]

[a] Bio-Based Chemistry Research Center, Advanced Convergent Chemistry Division, Korea Research Institute of Chemical Technology (KRICT), Ulsan 44429, Republic of Korea
[b] Department of Chemical Engineering, Dankook University, Yongin 16890, Republic of Korea
[c] Department of Chemistry, Sogang University, Seoul 04107, Republic of Korea
[d] Department of Chemical Engineering, Hanyang University, Seoul 04763, Republic of Korea
[e] Institute of Nano Science and Technology, Hanyang University, Seoul 04763, Republic of Korea

ARTICLE INFO

Article history:
Received 18 April 2020
Revised 22 May 2020
Accepted 25 May 2020
Available online 4 June 2020

Keywords:
Dye-sensitized solar cells
Donor-acceptor dyes
Electron-rich unit
Wide-range absorption
Impedance spectroscopy

ABSTRACT

Herein, we examine the performance of dye-sensitized solar cells containing five D-π-A organic dyes designed by systematic modification of π-bridge size and geometric structure. Each dye has a simple push-pull structure with a triarylamino group as an electron donor, bithiophene-4,4-dimethyl-4*H*-cyclopenta[1,2-*b*:5,4-*b*']dithiophene (**M11**), 4,4-dimethyl-4*H*-cyclopenta[1,2-*b*:5,4-*b*']dithiophene-thiophene (**M12**), thiophene-4,4-dimethyl-4*H*-cyclopenta[1,2-*b*:5,4-*b*']dithiophene (**M13**), 4,4-dimethyl-4*H*-cyclopenta[1,2-*b*:5,4-*b*']dithiophene-benzene (**M14**), and 4,4-dimethyl-4*H*-cyclopenta[1,2-*b*:5,4-*b*']dithiophene (**M15**) units as π-bridges, and cyanoacrylic acid as an electron acceptor/anchor. The extension of the π-bridge linkage favors wide-range absorption but, because of the concomitant molecular volume increase, hinders the efficient adsorption of dyes on the TiO_2 film surface. Hence, higher loadings are achieved for smaller dye molecules, resulting in (i) a shift of the TiO_2 conduction band edge to more negative values, (ii) a greater photocurrent, and (iii) suppressed charge recombination between the photoanode and the redox couple in the electrolyte. Consequently, under one-sun equivalent illumination (AM 1.5 G, 100 mW/cm^2), the highest photovoltage, photocurrent, and conversion efficiency (η = 7.19%) are observed for **M15**, which has the smallest molecular volume among **M** series dyes.

1. Introduction

Dye-sensitized solar cells (DSSCs) achieve high power conversion efficiencies at a relatively low cost and have therefore attracted much attention [1–9]. Among the DSSC components, dye sensitizers are of key importance for achieving high performance. Ru complex sensitizers such as **N3**, **N719**, and **N749** allow one to achieve power conversion efficiencies of >11% [2–7] but feature the drawbacks of high price and purification difficulty, therefore having limited commercialization potential [10]. Hence, metal-free organic dyes have been suggested as viable alternatives to Ru complexes, exhibiting the benefits of low cost, ease of purification, high molar extinction coefficients, and chemical structure tunability [11,12]. Moreover, the photovoltaic performance of these dyes has been gradually improved through the screening of numerous molecular structures, as exemplified by cyanine [13], merocyanine [14–16], coumarin [17,18], indoline [19,20], hemicyanine [21,22], triphenylamine [23–25], and xanthene [26] dyes, and can be further enhanced by extending dye absorption range and upgrading photoelectrochemical properties. Furthermore, a correlation between dye molecular structure and photovoltaic properties needs to be established.

The molecular design of dyes should preferentially consider their electronic properties, as a high molar extinction coefficient and narrow highest occupied molecular orbital (HOMO)-lowest unoccupied molecular orbital (LUMO) energy gap are required to realize high conversion efficiency DSSCs. Furthermore, the adsorbed dye molecules can influence the energetic and kinetic properties of the photoanode, e.g., the dipole moment of adsorbed dye molecules influences the surface potential of TiO_2 films, which results in an up- or downshift of the TiO_2 conduction band edge (CBE). Adsorbed dye molecules can also suppress charge recombination at the interface between the photoanode and redox couples in the electrolyte. Therefore, high dye loading is required to

---

* Corresponding authors at: Department of Chemical Engineering, Hanyang University, Seoul 04763, Republic of Korea.

E-mail addresses: dhlee@sogang.ac.kr (D.-H. Lee), mjko@hanyang.ac.kr (M.J. Ko).

[1] These authors contributed equally to this work.

https://doi.org/10.1016/j.jechem.2020.05.060

achieve efficient electron transport in DSSCs and high light harvesting efficiency. In addition, long alkyl groups may be introduced into organic dyes to prevent the approach of triiodide ions (I_3^-) to the surface of TiO_2 and thus hinder interfacial charge recombination [27]. For these reasons, it is important to study the influence of dye electronic properties and molecular structure on the photovoltaic properties of DSSCs for the design of highly efficient organic dyes.

Herein, we synthesize five D-π-A organic dyes designed by systematic modification of π-bridge size and molecular geometry. Each dye has a simple push–pull structure with a triarylamino group as an electron donor, bithiophene-4,4-dimethyl-4*H*-cyclopenta[1,2-*b*:5,4-*b*']dithiophene (**M11**), 4,4-dimethyl-4*H*-cyclopenta[1,2-*b*:5,4-*b*']dithiophene-thiophene (**M12**), thiophene-4,4-dimethyl-4*H*-cyclopenta[1,2-*b*:5,4-*b*']dithiophene (**M13**), 4,4-dimethyl-4*H*-cyclopenta[1,2-*b*:5,4-*b*']dithiophene-benzene (**M14**), and 4,4-dimethyl-4*H*-cyclopenta[1,2-*b*:5,4-*b*']dithiophene (**M15**) units as π-bridges, and cyanoacrylic acid as an electron acceptor/anchor (Fig. 1). The influence of the modified π-bridge on the electronic properties and molecular structure of organic dyes is examined, and the effect of the use of these dyes on the optical, energetic, and kinetic properties of the DSSC photoanode is investigated with a focus on dye loading, surface dipole moment, and interfacial charge recombination.

2. Experimental

2.1. Materials

All reagents and chemicals were purchased from Sigma-Aldrich or Alfa Aesar and used without further purification, unless otherwise stated. All solvents were dried and freshly distilled prior to use. All column chromatographic separations were performed using Merck silica gel (60–120 mesh).

2.2. DSSC fabrication

The synthesis of **M** series dyes is described in Supplementary Materials. Screen-printable pastes comprising TiO_2 nanoparticles (~20 nm) and large scattering TiO_2 particles (500 nm, G2, Showa Denko) were prepared as described elsewhere [28–30]. Fluorine-doped tin oxide (FTO) glass (8 Ω/sq, TEC-8, Pilkington) was cleaned with ethanol in an ultrasonic bath for 15 min and then subjected to 30-min UV-ozone treatment to remove residual impurities. A dense TiO_2 layer was coated on FTO glass by spin-casting of 7.5 wt% Ti(IV) bis(ethyl acetoacetato)diisopropoxide solution and annealed at 500 °C for 20 min. The TiO_2 nanoparticle paste was coated on the dense TiO_2 layer/FTO glass assembly by the doctor blade method and annealed at 500 °C for 30 min. Subsequently, the paste of scattering particles was coated on the annealed TiO_2 nanoparticle film and heated at 500 °C for 30 min. The resulting TiO_2 film, featuring a 10-µm-thick nanoparticle layer and a 5-µm-thick scattering particle layer, as determined by an Alpha-Step IQ surface profiler (KLA Tencor), was dipped into a 0.5 mM dye solution in anhydrous tetrahydrofuran (THF) for 12 h at room temperature (RT). To prepare the Pt counter electrode, a 0.65 mM solution of H_2PtCl_6 in isopropanol was drop-cast onto FTO glass and heated in air at 450 °C for 10 min. The dye-adsorbed TiO_2 film and the Pt/FTO glass counter electrode were assembled using a hot melt (Surlyn 1702, Dupont). Subsequently, an electrolyte drop was injected into the assembled cell through pre-drilled holes in the counter electrode. The photoanode active area was determined using a CCD camera (Moticam 1000) coupled with an image analysis program as 0.4–0.45 cm^2.

2.3. Measurements

UV–vis absorption spectra were recorded in a quartz cell with a path length of 1 cm (Agilent 8453). Photocurrent density–voltage

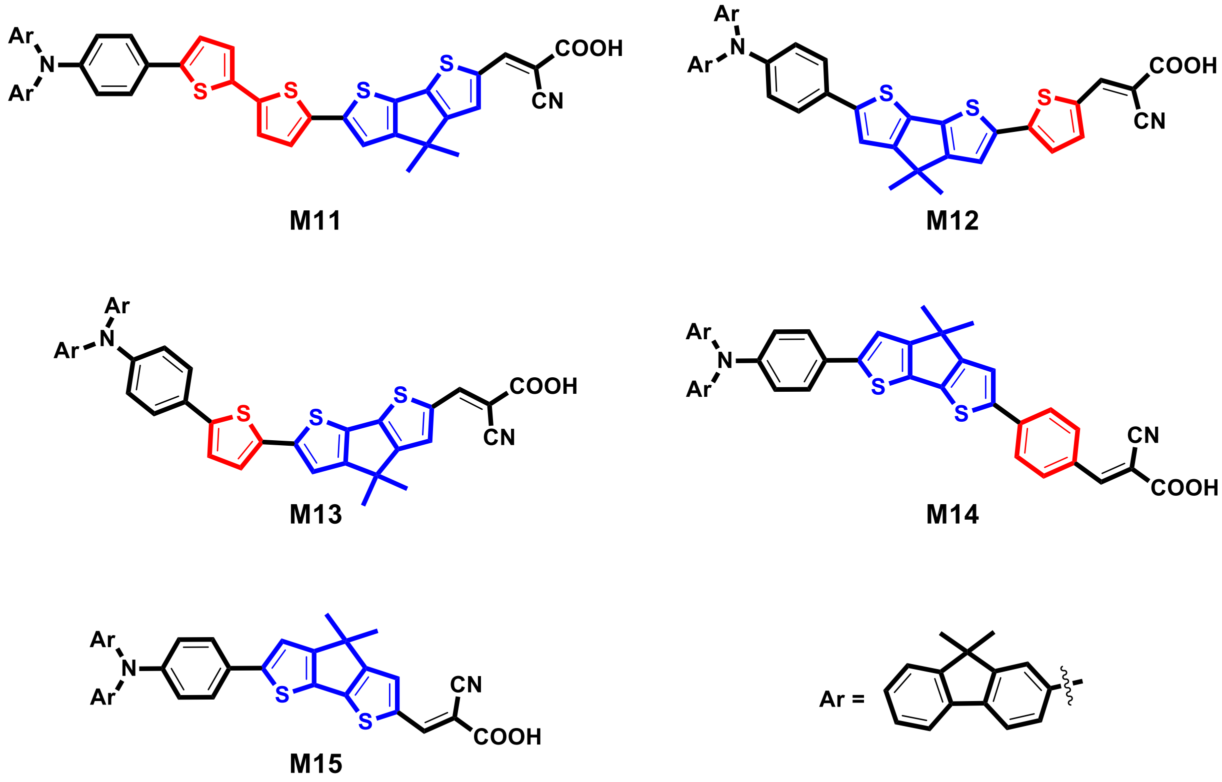

Fig. 1. Molecular structures of **M** series dyes.

(*J*–*V*) curves were obtained using a Keithley model 2400 source measurement unit. A solar simulator (Yamashita Denso YYS-200A) equipped with a 1000-W Xe lamp was utilized as a light source, and light intensity was adjusted to approximate that of 1 sun using a National Renewable Energy Laboratory–calibrated Si solar cell with a KG-5 filter. Prior to *J*–*V* measurements, DSSCs were covered by an aperture mask to screen additional illumination through the lateral space. Incident photon-to-current conversion efficiency (IPCE) spectra were obtained under short-circuit conditions at a spectral resolution of 10 nm using a Xe lamp and a grating monochromator (PV Measurements, Inc.). Electrochemical impedance spectra were recorded in the dark using a Solartron 1287 potentiostat at bias potentials from − 0.3 to − 0.6 V and a sinusoidal perturbation of 10 mV in the frequency range of 10^{-1}–10^5 Hz.

3. Results and discussion

3.1. Dye structures and syntheses

The molecular structures and synthetic routes of **M** series dyes are presented in Fig. 1 and Scheme 1, respectively. The synthesis of **M11** was initiated by the preparation of bromide **14** (Scheme 1). Pd-catalyzed Suzuki coupling of 2-([2,2′-bithiophen]-5-yl)-4,4,5,5-tetramethyl-1,3,2-dioxaborolane and **14** (65%) afforded **15b**, the boronylation of which by *n*-BuLi and 2-isopropoxy-4,4,5,5-tetramethyl-1,3,2-dioxaborolane provided dioxaborolane **16b** in 75% yield. The second Pd-catalyzed Suzuki coupling of **16b** and bromoaldehyde **7** (78%) followed by condensation of the thus obtained **17b** with cyanoacetic acid in the presence of piperidine (65%) afforded **M11**. Other **M** series dyes (**M12–15**) were synthesized in a similar way.

3.2. Optical properties

Fig. 2 shows the UV–vis absorption spectra of **M** series dyes in THF solution and on the TiO_2 film, with related optical data summarized in Table 1. As general D-π-A organic dyes, all **M** series dyes exhibited two broad peaks in near-UV and visible regions, corresponding to a π–π* transition and low-energy intramolecular charge transfer (ICT), respectively [31]. As listed in Table 1, the HOMO-LUMO energy gap ($E_{0\text{-}0}$) decreased with extension of the π-bridge linkage (except for **M11**), which facilitated wide-range absorption. The wavelengths of ICT absorption peak maxima (λ_{max} = 460–490 nm) in solution increased in the order of **M14** < **M11** < **M15** < **M13** < **M12** and hypsochromically shifted in

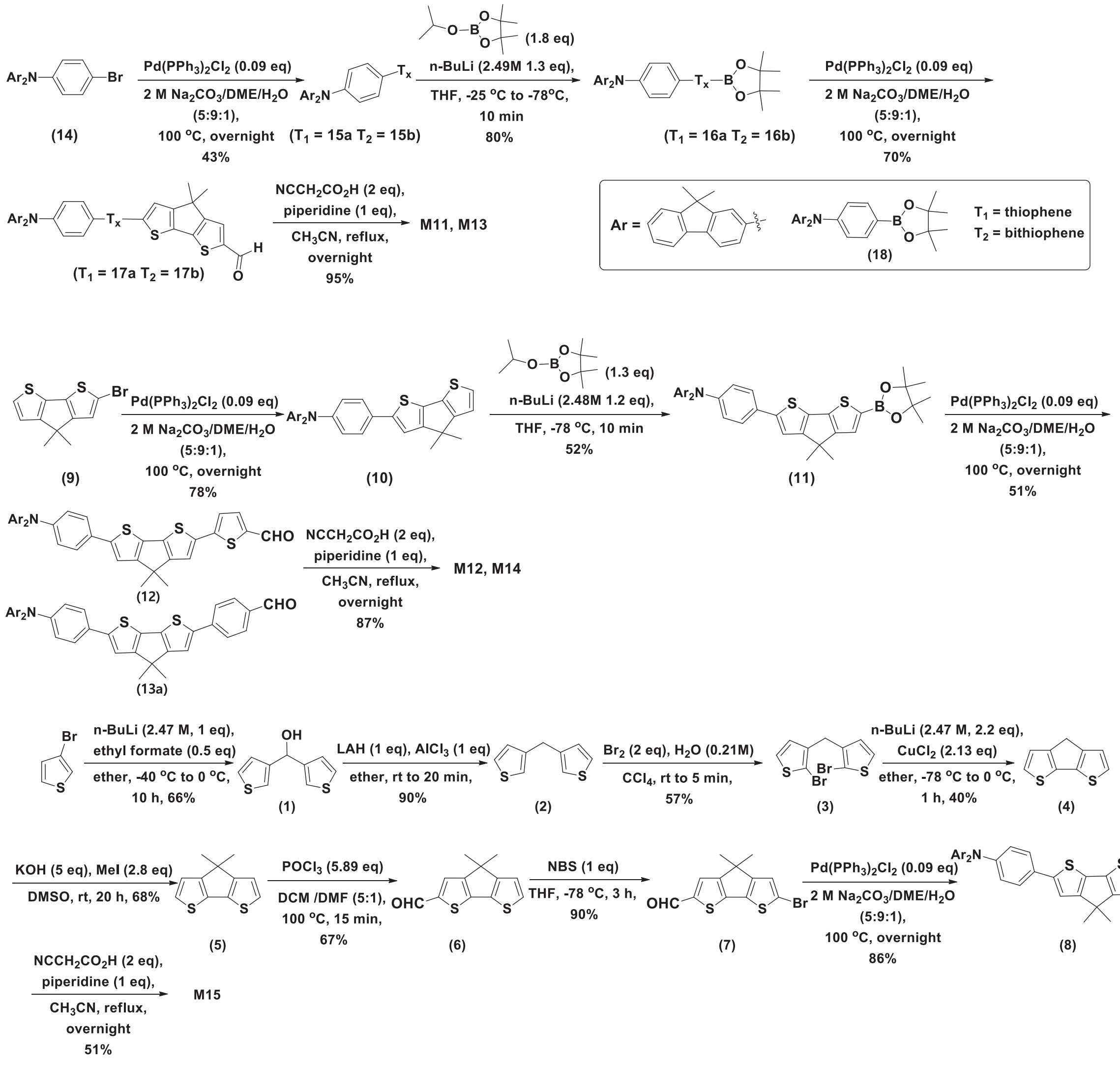

Scheme 1. Synthesis of **M** series dyes.

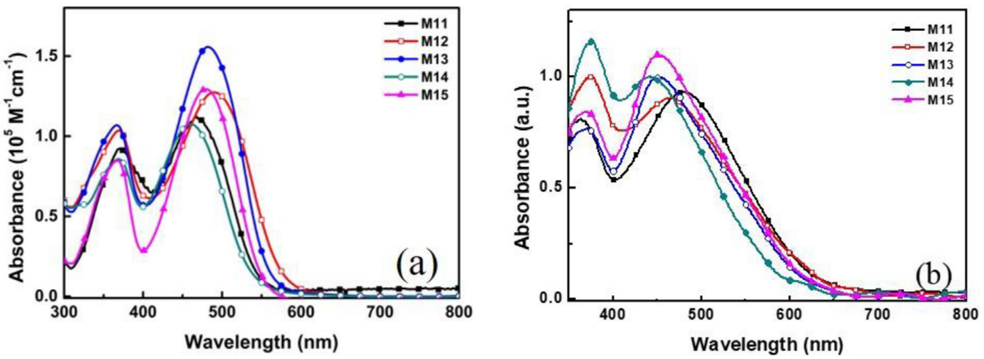

Fig. 2. Absorption spectra of **M** series dyes (a) in THF solution at a concentration of 10^{-5} M and (b) on 3-μm-thick nanocrystalline TiO_2 film.

Table 1
Optical and electrochemical properties of **M** series dyes.

Dye	λ_{max} (nm)[a]	ε (10^5 M^{-1} cm^{-1})	λ_{max} (nm) (on TiO_2)[b]	ε (10^5 M^{-1} cm^{-1}) (on TiO_2)	Dye loading (10^{-7} mol cm^{-2})	E_{ox}[c] vs. NHE (V)	$E_{0\text{-}0}$[d] (eV)	E_{ox}*[e] vs. NHE (V)
M11	468	1.12	478	0.93	4.3	1.04	2.17	−1.13
M12	490	1.27	465	0.91	2.1	1.05	2.06	−1.01
M13	482	1.56	450	1.00	4.8	1.15	2.14	−0.99
M14	460	1.08	442	0.99	4.5	1.15	2.19	−1.04
M15	480	1.29	450	1.10	7.9	1.06	2.21	−1.15

[a] Absorption spectra were recorded in THF solutions at 298 K.

[b] Absorption spectra were recorded on a nanocrystalline 3-μm-thick TiO_2 film.

[c] Redox potentials of **M** series dyes were measured in THF solution. Oxidation potentials were measured vs. Fc^+/Fc (E_{ox} = 0.85 V vs. Ag/Ag^+) and referenced to the NHE by addition of +0.63 V.

[d] $E_{0\text{-}0}$ is the optical band gap derived from the absorption onset in UV–vis spectra.

[e] E_{ox}* was calculated as $E_{0\text{-}0} - E_{ox}$.

the case of adsorption on the nanocrystalline TiO_2 film by 25, 32, 18, and 30 nm for **M12**, **M13**, **M14** and **M15**, respectively. Conversely, the absorption peak of **M11** was bathochromically shifted by 10 nm, which was ascribed to the interaction between the carboxylate group of this dye and Ti^{4+} in the TiO_2 electrode [32].

Compared to those measured in THF solution, the absorption onsets of **M** series dyes on the nanocrystalline TiO_2 film were red-shifted by 91, 98, 82, 74, and 120 nm for **M11**, **M12**, **M13**, **M14,** and **M15**, respectively (Fig. S1). This red-shift implies that *J*-aggregation was clearly dominant for **M** series dyes when adsorbed on the TiO_2 surface [33,34]. The amounts of dye molecules adsorbed on 10-μm-thick TiO_2 films were measured by desorption with NaOH solution, decreasing in the order of **M15** > **M13** > **M14** > **M11** > **M12** (Table 1). These results indicate that the extension of π-bridge linkage favored wide-range absorption but hindered efficient dye adsorption on TiO_2 films, as validated by theoretical calculations (see below). The large **M12** molecules adopted a widely spread conformation when adsorbed on the TiO_2 film surface (Fig. S2), which led to the adsorption of a relatively small amount of this dye. In addition, the molar extinction coefficient (ε) of the dyes adsorbed on the TiO_2 film was also influenced by their relative dye loading amount. As listed in Table 1, the greater dye loading led to the higher molar extinction coefficient of the dyes on the TiO_2 film. Furthermore, the red-shift in the absorption onsets of **M** series dyes on the TiO_2 film compared to that measured in THF solution (Fig. 2) was most pronounced for **M15** that exhibited the greatest dye loading. These results imply that the dye having a favorable molecular structure for the efficient adsorption on the TiO_2 film also exhibited a significant *J*-aggregation when adsorbed on the TiO_2 surface, leading to the higher molar extinction coefficient. The molecular structure of each **M** series dye will be discussed below.

3.3. Theoretical calculations

To compare the geometric and electronic structures of the five dye molecules, their HOMO and LUMO electron density surfaces were analyzed by density functional theory (DFT) calculations, which employed the B3LYP functional with the 6-31G* basis set (Fig. 3) [35]. In the optimized structure, the HOMO and LUMO electron distributions of all dyes were mainly located at the donor and acceptor, respectively, i.e., HOMO-LUMO excitation could effectively occur upon irradiation with light and was expected to be accompanied by an electron shift from the donor moiety to the acceptor moiety. For conformational investigation, we evaluated the dihedral angles between the donor unit and adjacent π-bridge units for all dyes (Fig. 3). In particular, **M12** had a particularly small dihedral angle (4.2°) between 4,4-dimethyl-4*H*-cyclopenta[1,2-*b*:5,4-*b*']dithiophene and thiophene units, having a more planar geometry than other dyes. This planar geometry resulted in additionally extended π-conjugation and, consequently, in the smallest HOMO-LUMO energy gap in the **M** series.

3.4. Electrochemical properties

The efficient injection of electrons from the dye to the TiO_2 conduction band as well as effective dye regeneration are essential for high DSSC performance. The driving force for dye regeneration is determined by the energy gap between the dye HOMO and the redox potential of I^-/I_3^- in the electrolyte (0.35 V vs. normal hydrogen electrode, NHE) [36]. The oxidation potentials (E_{ox}) corresponding to dye HOMO levels were measured by cyclic voltammetry in THF solution (Fig. S3) as 1.04–1.15 V vs. NHE, decreasing in the order of **M14** ≈ **M13** > **M15** > **M12** > **M11** and being sufficiently low to accelerate dye regeneration by the I^-/I_3^-

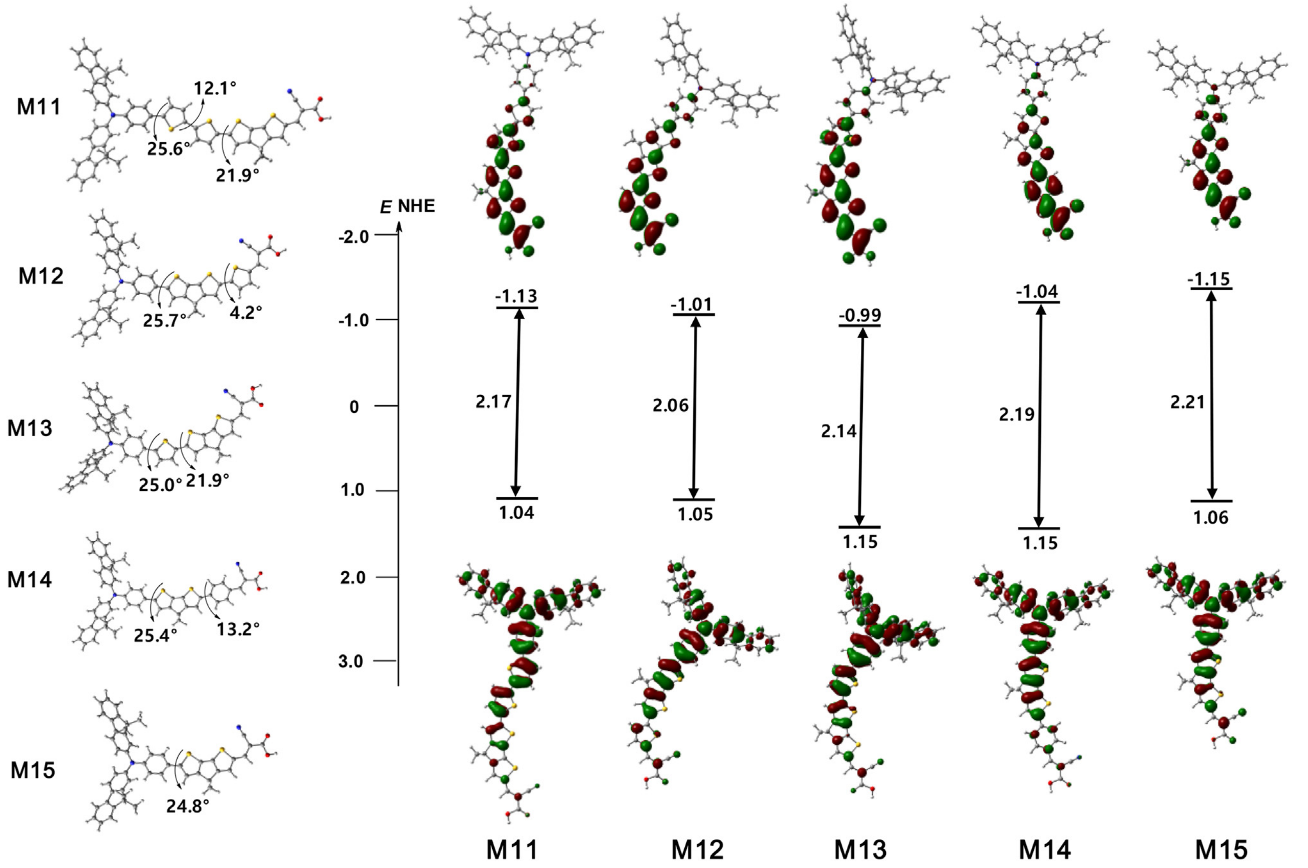

Fig. 3. Optimized structures and HOMO/LUMO electron distributions of **M** series dyes.

redox couple [37]. The LUMO levels were calculated by subtracting $E_{0\text{-}0}$ values from the HOMO levels, with values of $-$ 1.13, $-$1.01, $-$0.99, $-$1.04, and $-$1.15 V vs. NHE obtained for **M11**, **M12**, **M13**, **M14**, and **M15**, respectively (Table 1). Considering that the conduction band edge (CBE) of TiO_2 equals $-$0.28 V vs. NHE, these LUMO levels were sufficiently high for achieving efficient electron injection to TiO_2 [38].

3.5. Photovoltaic performance of DSSCs

Fig. 4 presents the IPCE spectra of DSSCs with **M** series dyes as sensitizers, revealing that each dye exhibited a maximum IPCE value in the range of 47%–77% and an absorption onset at 730–780 nm. The absorption onset order well matched that observed for the UV–vis absorption spectra of dyes adsorbed on TiO_2 film (Fig. 2b). The maximum IPCE values were strongly affected by the amount of dye loaded on the photoanode. Although **M12** exhibited the broadest absorption spectrum due to the narrowest HOMO-LUMO gap, it showed the lowest maximum IPCE value because of a particularly low dye loading [39,40]. On the other hand, **M15** showed the highest maximum IPCE value because of its remarkably high loading. Given that all employed dyes had similar absorption coefficients (α), as shown in Table 1, it is reasonable that the relative light harvesting efficiency and the resulting IPCE value for each DSSC were largely determined by dye loading.

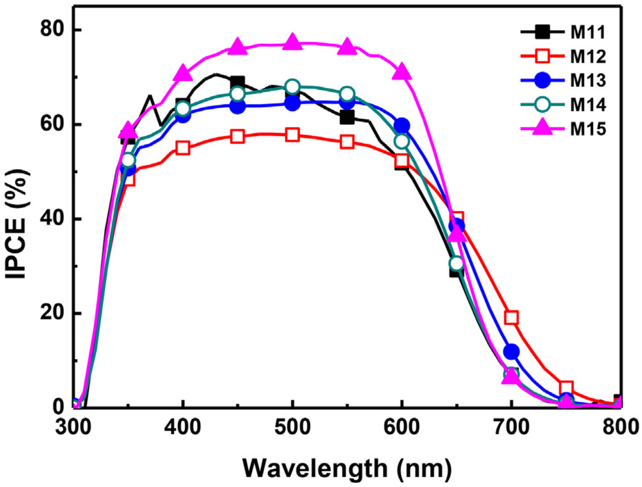

Fig. 4. IPCE spectra of DSSCs with **M** series dyes.

The photocurrent density–voltage (J–V) curves of DSSCs under illumination are shown in Fig. 5, and the related photovoltaic parameters are listed in Table 2. For statistical significance, all parameters in Table 2 were averages from three different cells for each dye, with the exception of the champion cell. In addition, the complete data set is available in Table S1. The trend of short-circuit photocurrent (J_{SC}) well agreed with that of IPCE spectra, e.g., **M15** exhibited the highest J_{SC} due to the largest dye loading. The open-circuit voltage (V_{OC}) and fill factor (FF) were also strongly influenced by dye loading. **M12** showed the lowest V_{OC}, while **M15** exhibited the highest V_{OC} and *FF*. The dependence of V_{OC} and *FF* on dye loading was closely related to the electron recombination rate in the DSSC (see section on electrochemical impedance spectroscopy (EIS)). As a result, conversion efficiencies of 4.79, 4.45, 5.04, 4.98, and 7.14% were obtained for **M11**, **M12**, **M13**, **M14**, and **M15**, respectively. In addition, the champion cell employing **M15** exhibited a conversion efficiency of 7.19%.

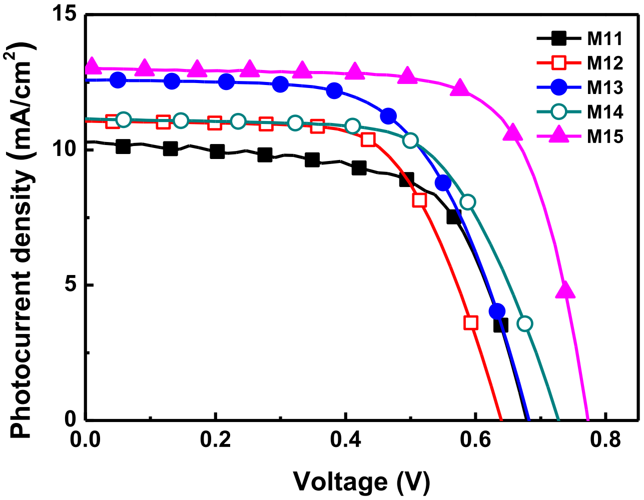

Fig. 5. Photocurrent density–voltage (*J*–*V*) curves of DSSCs with **M** series dyes.

3.6. Relationship between surface dipole moment and CBE shift

The TiO_2 CBE can be shifted by modification of the surface potential of TiO_2 films, e.g., as a result of a change in ion adsorption or pH [38]. Similarly, the CBE (and hence, V_{OC}) is also affected by the dipole moment of dye molecules and the electrolyte cations adsorbed on the TiO_2 film. Therefore, we calculated the dipole moments of dye molecules using the B3LYP functional with the 6-31G* basis set to investigate the effect of this parameter on V_{OC}. First, the carboxylate group of each dye was assumed to bond to TiO_2 in a bidentate mode perpendicularly to the TiO_2 surface, with the vertical axis denoted as the *z*-axis and the horizontal axis denoted as the *y*-axis. Second, the coverage of dipole values on TiO_2 surfaces was implicitly evaluated by dye loading, which was calculated by desorption of dyes adsorbed on TiO_2 film using a NaOH solution. The change in TiO_2 CBE, ΔCBE, can be expressed as [41]

$$\Delta CBE = \frac{N\left|\vec{\mu}_{tot}\right|\cos\theta}{\varepsilon\varepsilon_0} \quad (1)$$

where *N* is the number of dipoles (equivalent to surface concentration), $\vec{\mu}_{tot}$ is the dipole moment vector, θ is the tilt angle between $\vec{\mu}_{tot}$ and the normal direction of the TiO_2 surface, ε is the permittivity of the dipole layer, and ε_0 is the permittivity of free space [42]. Both the direction and magnitude of $\vec{\mu}_{tot}$ can affect ΔCBE. The product of $\vec{\mu}_{tot}$ and cosθ corresponds to the absolute magnitude of the dipole moment component (μ_z) perpendicular to the TiO_2 film, and the direction is indicated from negative to positive charges.

The above calculations showed that for all dyes, the dipole moments point away from the TiO_2 surface (Fig. 6), i.e., a negative TiO_2 surface potential is induced. ΔCBE (vs. NHE) is positively correlated with the absolute value of this negative surface potential, and, hence, with V_{OC} because of the upward shift of TiO_2 conduction bands. The coverage of the dipole moment of a single dye molecule and that of the dipole itself strongly influence CBE shift. Therefore, for the evaluation of *N*, the parameters summarized in Table 1 were used to determine dye loading. Although the μ_z of **M15** was lower than that of **M14**, the ΔCBE of the former was higher than that of the latter, which suggests that the change in TiO_2 CBE potential is strongly governed by the amount of dye molecules. As a result, ΔCBE increased in the order of **M12** < **M11** < **M13** < **M14** < **M15** (Table 3).

In addition to the magnitude of a single dipole moment, the total number of dipole moments (and hence, the amount of dye loaded on TiO_2) also influences the ΔCBE of the photoanode. Herein, we performed DFT calculations to elucidate the origin of the variability of adsorbed dye loading, which was believed to be associated with dye molecular structure. Based on DFT-optimized conformations (Fig. S4), we evaluated the molecular volumes of single dye molecules on the TiO_2 surface. Considering the rotation of dye molecules around the bidentate anchoring axis, a dye with a greater tilting angle with respect to the TiO_2 surface may have a larger molecular volume, thus strongly sterically hindering the adsorption of another dye on adjacent sites. In practice, dye loading was found to be inversely proportional to molecular volume (Table S2). The largest molecular volume (**M12**) was 3.05 times greater than the smallest one (**M15**), while the loading of **M15** was 3.76 times greater than that of **M12**.

3.7. EIs

The effects of charge transfer behavior on photovoltaic performance were probed by EIS. Impedance spectra obtained for DSSCs employing each dye in the dark at bias potentials between − 0.3 and − 0.6 V were and fitted using ZView software. The equivalent circuit model comprised a series resistance (R_S), impedance at the electrolyte/counter electrode interface (R_{Pt} and CPE_1), and impedance at the electrolyte/photoanode interface (R_{ct} and CPE_2) (Fig. S5) [43].

The constant phase element (CPE) is generally employed for electrodes with a relatively rough surface instead of typical capacitance and was herein used to evaluate the chemical capacitance (C_μ) of the photoanode. Fig. 7 presents the thus calculated C_μ, interfacial charge resistance (R_{ct}), and electron lifetime (τ_n) as functions of the bias potential (τ_n can be determined as the product of R_{ct} and C_μ) [44]. As shown in Fig. 7(a), C_μ increased in the order of **M15** < **M14** < **M13** < **M11** < **M12** at constant bias potential, i.e., the shift of ΔCBE became progressively less negative in the same order. These results were in good agreement with experimental data, and the observed trend was attributed to the influence of the dipole moment and amount of adsorbed dye molecules on the TiO_2 electrode [45]. As shown in Fig. 7(b), R_{ct} increased in the

Table 2
Photovoltaic performance of DSSCs with **M** series dyes.[a]

Dye	J_{SC} (mA/cm^2)	V_{OC} (mV)	FF	η (%)
M11[b]	10.60 ± 0.11	674 ± 2	0.671 ± 0.010	4.79 ± 0.07
M12[b]	10.70 ± 0.36	652 ± 12	0.638 ± 0.007	4.45 ± 0.14
M13[b]	12.07 ± 0.50	693 ± 12	0.602 ± 0.011	5.04 ± 0.22
M14[b]	10.50 ± 1.06	729 ± 31	0.650 ± 0.025	4.98 ± 0.24
M15[c]	13.09 ± 0.08	774 ± 4	0.705 ± 0.009	7.14 ± 0.05
Champion cell (M15)	13.03	773	0.714	7.19

[a] Photovoltaic performance was evaluated under irradiation with AM 1.5 G simulated solar light (100 mW/cm^2). All parameters were averaged from there different devices. The concentration of **M** series dyes (in THF) was 0.5 mM.

[b] 0.5 mM in THF and 0.6 M 1-propyl-3-methylimidazoliumiodide, 0.1 M LiI, 0.03 M I_2, 0.5 M 4-*tert*-butylpyridine (TBP) in acetonitrile as electrolyte.

[c] 0.6 M tetrabutylammonium iodide, 0.1 M LiI, 0.05 M I_2, 0.5 M TBP in acetonitrile as electrolyte.

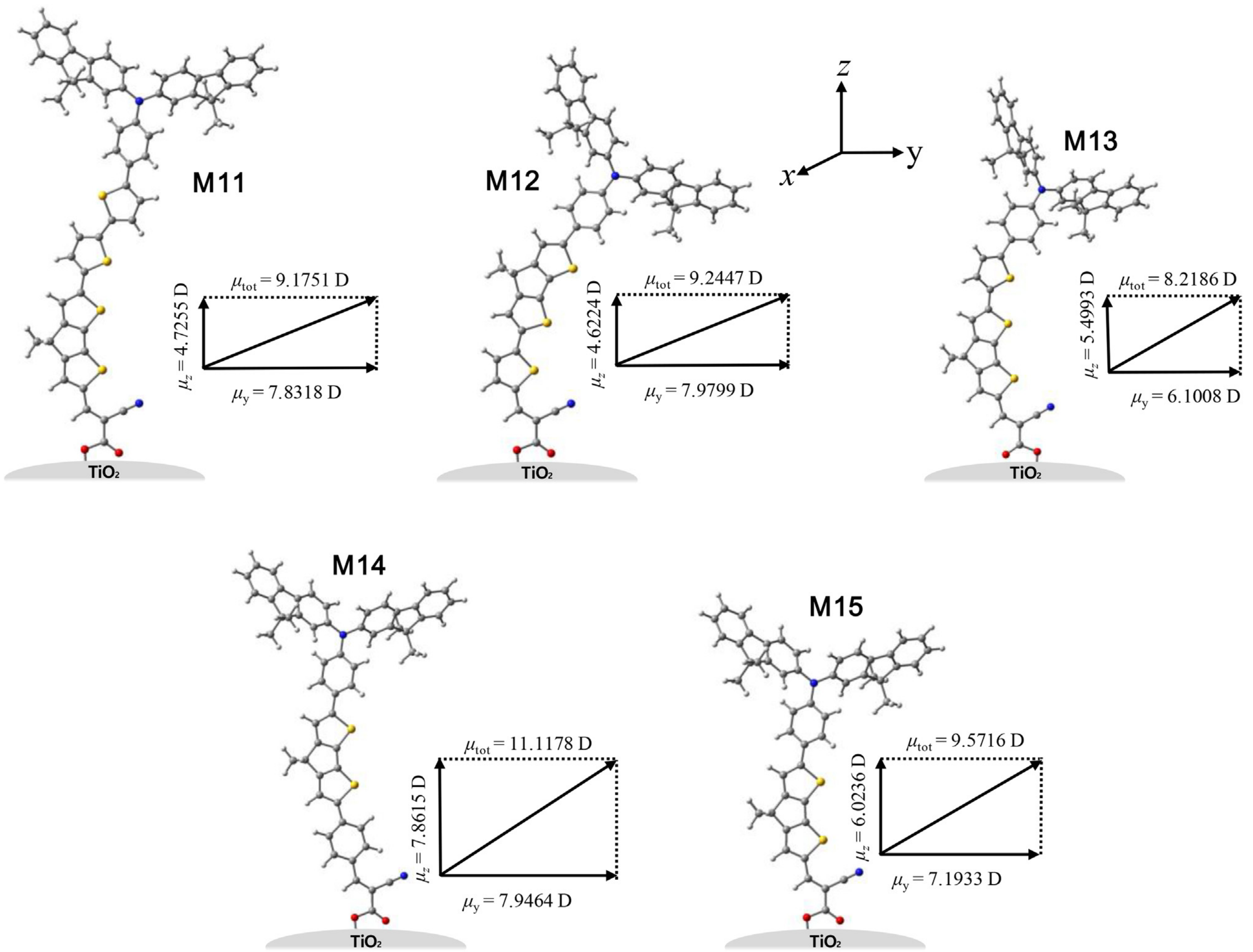

Fig. 6. Optimized dipole moment analysis of **M** series dyes in the free state and in bidentate binding mode. The molecular plane is perpendicular to the TiO_2 surface plane, the *z*- and *y*-axes are the normal and horizontal components, respectively.

Table 3
Calculated Δ*CBE* of TiO_2 electrodes with **M** series dyes.

Dye	$\vec{\mu}_{tot}$	cos θ	μ_z	N	ΔCBE [a]
M11	9.1751	59	4.7255	4.3×10^{-7}	1
M12	9.2447	60	4.6224	2.1×10^{-7}	0.48
M13	8.2186	48	5.4993	4.8×10^{-7}	1.30
M14	11.1178	45	7.8615	4.5×10^{-7}	1.74
M15	9.5716	51	6.0236	7.9×10^{-7}	2.34

[a] Each value of ΔCBE was normalized by that of **M11**.

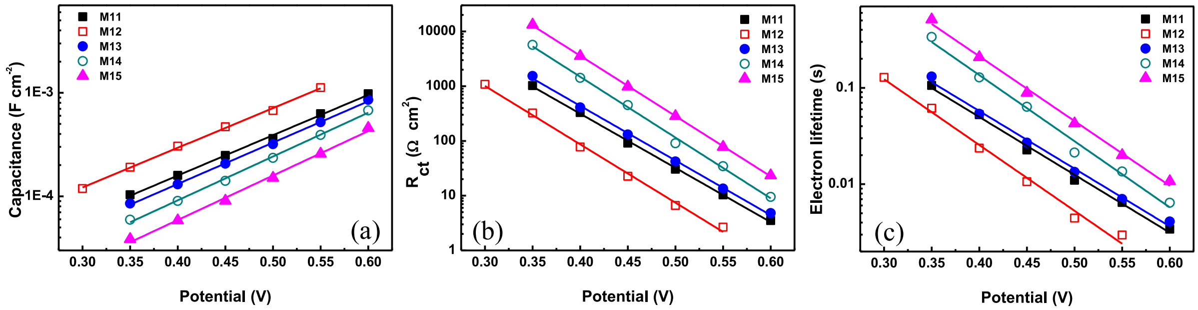

Fig. 7. (a) Chemical capacitances, (b) recombination resistances, and (c) electron lifetimes obtained from the impedance spectra of DSSCs with **M** series dyes in the dark state.

order of **M12** < **M11** < **M13** < **M14** < **M15**, which matches the order of the amount of dye molecules adsorbed on the TiO_2 surface (Table 1). The R_{ct} values of **M15** were 1–3 orders greater compared to those of **M12** that showed the lowest dye loading amount over the entire range of applied potential. As R_{ct} is closely associated with the degree of suppression of electron recombination at the TiO_2/electrolyte interface, it is reasonable that the adsorbed layer of **M15** was significantly more compact than that of other dyes. This compact layer on the TiO_2 surface prevented I_3^- ions from directly approaching the exposed TiO_2 surface, suppressing electron recombination at the interface of the TiO_2 film and the electrolyte [46]. As a result, electron lifetime followed the same trend as R_{ct} (Fig. 7c). The electron lifetime of **M15** was 10–20 times higher compared to that of **M12** over the entire range of applied potential. These data imply that the inferior photovoltaic performances of **M11**–**14** compared to that of **M15** primarily result from the lower electron lifetimes (due to the smaller amount of adsorbed dye molecules) of the former dyes.

In our previous study, organic dyes with similar D-π-A structure, named **M9** and **M10**, were developed for application in DSSCs [47]. For **M9** and **M10**, thieno[3,2-b]thiophene and EDOT units were incorporated as π-bridges. In particular, **M10** showed a relatively high conversion efficiency (η = 7.00%) because of its low electron recombination rate caused by the blocking effect of the bulky EDOT moiety. Compared to these two dyes, **M11**–**14** exhibited smaller HOMO-LUMO energy gaps due to their longer π-conjugation length, and **M15** showed similar HOMO-LUMO energy gap because of its relatively short π-conjugation length. However, **M15** showed much higher dye loading compared to that of **M10**, because of its simple structure and small molecular volume. In addition, **M15** exhibited a higher V_{OC} (773.0 mV for **M15** and 731.8 mV for **M10**) and a comparable electron lifetime compared to those of **M10**, leading to a slightly higher conversion efficiency. These results imply that the compact adsorption of dyes on the photoanode is as effective as the incorporation of bulky moiety for reducing the electron recombination rate in the DSSCs.

Although **M12** showed the lowest conversion efficiency in this work due to its unfavorable molecular structure for the high loading on the TiO_2 film, it has a potential advantage of a narrow HOMO-LUMO energy gap that is essential for the wide-range absorption of visible light. Therefore, with a proper modification of the molecular structure, highly efficient D-π-A organic dyes could be developed. For instance, if spacer or aromatic moieties with a more planar structure are introduced, the tilting angle of **M12** can be reduced, resulting in an enhanced dye loading. In other way, the photovoltaic performances of **M15** also can be enhanced by introducing more electron-rich moieties as a spacer, such as thiophene or selenophene, maintaining its small molecular volume [48]. By introducing these electron-rich units, the HOMO-LUMO energy gap of **M15** can be reduced, leading to the wide-range absorption of visible light.

4. Conclusions

Five organic dyes with D-π-A structure comprising a triarylamine unit as the electron donor, cyanoacrylic acid as the anchoring unit, and 4,4-dimethyl-4*H*-cyclopenta[1,2-*b*:5,4-*b*']dithiophene substituted with benzene or thiophene derivatives as the π-bridge were synthesized. The extension of π-bridge linkage decreased the HOMO-LUMO gap and thus facilitated wide-range absorption. However, dyes with an extended π-bridge featured a higher molecular volume, which resulted in decreased dye loading on the TiO_2 surface. DFT calculations and EIS revealed that higher dye loading leads to (i) a shift of the TiO_2 CBE to more negative values, (ii) a greater photocurrent of the corresponding DSSCs, and (iii) suppressed charge recombination between the photoanode and the redox couple in the electrolyte. Consequently, the highest photovoltage, photocurrent, and conversion efficiency were achieved for **M15** (which has the smallest molecular volume among **M** series dyes) despite its large HOMO-LUMO gap. The obtained results provide valuable insights into the molecular design of organic dyes for highly efficient photovoltaics.

Declaration of Competing Interest

The authors declare that they have no known competing financial interests or personal relationships that could have appeared to influence the work reported in this paper.

Acknowledgments

This work was supported by Basic Science Research through the National Research Foundation of Korea (NRF) funded by the Ministry of Education (No. 2017R1D1A1B03035077). This work is also supported by Research Program (2018R1A2B2006708) and Technology Development Program to Solve Climate Changes (2015M1A2A2057062) funded by the National Research Foundation under the Ministry of Science and ICT, Republic of Korea. This research was supported by the Defense Challengeable Future Technology Program of the Agency for Defense Development, Republic of Korea.

Appendix A. Supplementary data

Supplementary data to this article can be found online at https://doi.org/10.1016/j.jechem.2020.05.060.

References

[1] B. O'Regan, M. Grätzel, Nature 353 (1991) 737–740.
[2] M.K. Nazeeruddin, A. Kay, I. Rodicio, R.H. Baker, E. Muller, P. Liska, N. Vlachopoulos, M. Grätzel, J. Am. Chem. Soc. 115 (1993) 6382–6390.
[3] M.K. Nazeeruddin, P. Péchy, T. Renouard, R.H. Zakeeruddin, P. Baker, P. Comte, L. Liska, E. Cevey, V. Costa, L. Shklover, G.B. Spiccia, C.A. Deacon, C.A. Bignozzi, M. Grätzel, J. Am. Chem. Soc. 123 (2001) 1613–1624.
[4] T. Renouard, R.A. Fallahpour, M.K. Nazeeruddin, R. Humphr, S.I. Gorelsky, A.B.P. Leve, M. Grätzel, Inorg. Chem. 41 (2002) 367–378.
[5] Y. Masatoshi, Y. Takeshi, K. Mitsuhiko, H. Kohjiro, K. Ryuzi, S. Hideki, A. Hironor, Inorg. Chem. 42 (2003) 7921–7931.
[6] K. Carmen, K.N. Mohammad, D.C. Davide, L. Paul, G. Micheal, Inorg. Chem. 43 (2003), 4216 4126.
[7] H. Tributsch, Coord. Chem. Rev. 248 (2004) 1511–1530.
[8] Y. Li, D.K. Lee, J.Y. Kim, B.S. Kim, N.G. Park, K. Kim, J.H. Shin, I.S. Choi, M.J. Ko, Energy Environ. Sci. 5 (2012) 8950–8957.
[9] Y. Li, S.C. Palacios, K. Yoo, J.H. Kim, A. Jiménez-Solano, C.H. Lee, H. Míguez, M.J. Ko, Energy Environ. Sci. 9 (2016) 2061–2071.
[10] Y. Numata, A. Islam, H. Chen, Energy Environ. Sci. 5 (2015) 8548–8552.
[11] K. Pei, Y. We, A. Islam, Q. Zhang, L. Han, H. Tian, W. Zhu, ACS Appl. Mater. Interfaces 5 (2013) 4986–4995.
[12] W. Ying, J. Yang, M. Wielopolski, T. Moehl, J. Moser, P. Comte, J. Hua, S. Zakeeruddin, H. Tian, M. Grätzel, Chem. Sci. 5 (2014) 206–214.
[13] S. Ferrere, A. Zaben, B.A. Gregg, J. Phys. Chem. B 101 (1997) 4490–4493.
[14] A.C. Khazraji, S. Hotchandani, S. Das, P.V. Kamat, J. Phys. Chem. B 103 (1999) 4693–4700.
[15] K. Sayama, K. Hara, N. Mori, M. Satsuki, S. Suga, S. Tsukagoshi, Y. Abe, H. Sugihara, H. Arakawa, Chem. Commun. (2000) 1173–1174.
[16] K. Sayama, S. Tsukagoshi, T. Mori, K. Hara, Y. Ohga, A. Shinpou, Y. Abe, S. Suga, H. Arakawa, Sol. Energy Mater Sol. Cells 80 (2003) 47–71.
[17] K. Hara, K. Sayama, Y. Ohga, A. Shinpo, S. Suga, H. Arakawa, Chem. Commun. (2001) 569–570.
[18] K. Hara, Z.S. Wang, T. Sato, A. Furube, R. Katoh, H. Sugihara, O.Y. Dan, C. Kasada, A. Shinpo, S. Suga, J. Phys. Chem. B 109 (2005) 15476–15482.
[19] T. Horiuchi, H. Miura, S. Uchida, Chem. Commun. (2003) 3036–3037.
[20] T. Horiuchi, H. Miura, K. Sumioka, S. Uchida, J, Am. Chem. Soc. 126 (2004) 12218–12227.
[21] Z.S. Wang, F.Y. Li, C.H. Huang, Chem Commun. (2000) 2063–2064.
[22] Q.H. Yao, F.S. Meng, F.Y. Li, H. Tian, C.H. Huang, J. Mater. Chem. 13 (2003) 1048–1053.
[23] M. Velusamy, K.R.J. Thomas, J.T. Lin, Y.C. Hsu, K.C. Ho, Org. Lett. 7 (2005) 1899–1902.

[24] T. Kitamura, M. Ikeda, K. Shigaki, T. Inoue, N. Anderson, X. Ai, T. Lian, S. Yanagida, Chem. Mater. 16 (2004) 1806–1812.
[25] D.P. Hagberg, T. Edvinsson, T. Marinado, G. Boschloo, A. Hagfeldt, L. Sun, Chem. Commun. (2006) 2245–2247.
[26] K. Hara, T. Horiguchi, T. Kinoshita, K. Sayama, H. Sugihara, H. Arakawa, Chem. Lett. 4 (2000) 316–317.
[27] N. Koumura, Z.S. Wang, S. Mori, M. Miyashita, E. Suzuki, K. Hara, J. Am. Chem. Soc. 128 (2006) 14256–14257.
[28] H.J. Koo, J. Park, B. Yoo, K. Yoo, K. Kim, N.G. Park, Inorg. Chim. Acta. 361 (2008) 677–683.
[29] J.A. Lee, J.Y. Kim, W. Kim, S.H. Kang, M.J. Ko, Int. J. Precis. Eng. Manuf-Green Technol. 7 (2020) 69–76.
[30] J.Y. Kim, J. Yang, J.H. Yu, W. Baek, C.H. Lee, H.J. Son, T. Hyeon, M.J. Ko, ACS Nano 9 (2015) 11286–11295.
[31] S. Roquet, A. Cravino, P. Leriche, O. Alévêque, P. Frère, J. Roncali, J. Am. Chem. Soc. 128 (2006) 3459–3466.
[32] Z.S. Wang, K. Hara, O.Y. Dan, C. Kasada, A. Shinpo, S. Suga, H. Arakawa, H. Sugihara, J. Phys. Chem. B 109 (2005) 3907–3914.
[33] W. Zhu, Y. Wu, S. Wang, W. Li, X. Li, J. Chen, Z.S. Wang, H. Tian, Adv. Funct. Mater. 21 (2011) 756–763.
[34] M.W. Lee, J.Y. Kim, H.J. Son, J.Y. Kim, B. Kim, H. Kim, D.K. Lee, K. Kim, D.H. Lee, M.J. Ko, Sci. Rep. 5 (2015) 7711.
[35] P.J. Stephens, F.J. Devlin, C.F. Chablowski, M. Frisch, J. Phys. Chem. 98 (1994) 11623–11627.
[36] A. Listorti, B. O'Regan, J.R. Durrant, Chem. Mater. 23 (2011) 3381–3399.
[37] J.N. Clifford, E. Palomares, M.K. Nazeeruddin, M. Grätzel, J.R. Durrant, J. Phys. Chem. C 111 (2007) 6561–6567.
[38] M. Grätzel, Nature 414 (2001) 338–344.
[39] B.C. O'Regan, K. Walley, M. Juozapavicius, A. Anderson, F. Matar, T. Ghaddar, S. M. Zakeeruddin, C. Klein, J.R. Durrant, J. Am. Chem. Soc. 131 (2009) 3541–3548.
[40] S.E. Koops, B.C. O'Regan, P.R.F. Barnes, J.R. Durrant, J. Am. Chem. Soc. 131 (2009) 4808–4818.
[41] J. Kruger, U. Bach, M. Grätzel, Adv. Mater. 12 (2000) 447–451.
[42] S.M. Sze, Semiconductor devices, Wiley, New York, 1985.
[43] F. Fabregat-Santiago, J. Bisquert, G. Garcia-Belmonte, G. Boschloo, A. Hagfeldt, Sol. Energy Mater. Sol. Cells 87 (2005) 117–131.
[44] F. Fabregat-Santiago, G. Garcia-Belmonte, I. Mora-Seró, J. Bisquert, Phys. Chem. Chem. Phys. 13 (2011) 9083–9118.
[45] Z. Wang, M. Liang, Y. Hao, Y. Zhang, L. Wang, Z. Suna, S. Xue, J. Mater. Chem. A 1 (2013) (1819) 11809–11811.
[46] S.R. Li, C.P. Lee, H.T. Kuo, K.C. Ho, S.S. Sun, Chem. Eur. J. 18 (2012) 12085–12095.
[47] M.W. Lee, J.Y. Kim, D.H. Lee, M.J. Ko, A.C.S. Appl, Mater. Interfaces 6 (2014) 4102–4108.
[48] R. Li, X. Lv, D. Shi, D. Zhou, Y. Cheng, G. Zhang, P. Wang, J. Phys. Chem. C 113 (2009) 7469–7479.